Best Focus Shift Mechanism for Thick Masks

Martin Burkhardt[a], Ananthan Raghunathan[b]

[a] IBM Research, Yorktown Heights, NY, [b] IBM SRDC, Hopewell Junction, NY

ABSTRACT

The best focus shift due to thick mask effects is well known, both in ArF, and more importantly in EUV, where the shorter wavelength is small compared to both mask openings and absorber height. While the effect is stronger in opaque features in clear field masks, the best focus shift is visible in dark field masks as well, and it becomes even more pronounced when scattering bars are added to non-dense features. This pattern dependent focus variation can be predicted in both exact EMF simulations and fast image calculations that are used for optical proximity correction (OPC).

Even though this focus shift can be predicted and patterns can be corrected in OPC, we would like to understand the mechanism that causes this focus shift. This can help us understand if, in addition to best focus shift, the image quality is further deteriorated due to the thick mask effects. The best focus shift is found to be an interplay of the complex diffraction coefficient due to thick mask effects and the direction of the light that is incident on the mask, or coherence value σ. A change in focus adds a phase term to each of the complex diffraction coefficients, causing their rotation in a phasor diagram. Best focus is found when the phasors have an angle of 0 or 180 degrees to each other and depending on which diffracted orders are caught in the pupil and contribute to imaging. We investigate the effect of partial coherence, mask thickness, and assist feature placement on best focus shift. We observe a waveguide effect in the absorber gaps because of the reduced real index of refraction in the absorber layer, making vacuum the optically dense medium. We suggest ways to lessen the best focus shifts through assist feature placement or the use of alternative absorbers that are closer matched to the dielectric index of vacuum.

Keywords: EUV, Thick Mask, Assist Features, Bossung Tilt, Focus Shift, Waveguide, Absorber, Defects

1. INTRODUCTION

EUV is a strong candidate for BEOL patterning at the 7 nm node. Among the possible pitches for this node, we chose a base pitch of 36 nm to investigate the effect of assist features on trench printing at non-dense pitches, such as 2× and 3× the minimum pitch. The dense pitch of 36 nm corresponds to a k_1 of 0.44, which would not be considered aggressive for ArF lithography, but which is a value at which assist features have been introduced in the past for both KrF and ArF lithography. The k_1 value can be considered aggressive for EUV due to it's less mature resist systems and elevated flare. We are interested in whether or not the insertion of assist features provides for an overall increase in the process window or if focus shift effects lead to a decrease in common depth of focus. For this, we would like to know what causes and influences the magnitude of the best focus shift, and with this we may find some methods to suppress it's negative impact. In earlier work, Krautschik et al.[1] have investigated Bossung curve asymmetry and best focus effects, which were found to be strong for opaque features in clear field masks.[2] Other work has shown that dark field patterning of trenches is relatively immune to such focus shift effects.[3,4]

In earlier work,[5] we reported on best focus shift of trenches after addition of clear assist features to non-nested gratings. Figure 1 compares the Bossung curves for 72 nm pitch trenches, printing at roughly 20 nm for the non-assisted case on the left, and slightly larger for the assisted case on the right. The main features are designed as 23 nm openings at 72 nm pitch in wafer dimensions, and the assist features were nominally 10 nm in size, but due to process bias on the mask came out closer to 8.5 nm in wafer dimensions. For this reason, most simulations in this paper use an assist feature size of 8 nm. There is a strong focus shift of more than 50 nm after addition of the assist feature. The insert on the left shows the quasar illumination that is used in

email: martburk@us.ibm.com

Extreme Ultraviolet (EUV) Lithography VI, edited by Obert R. Wood II, Eric M. Panning,
Proc. of SPIE Vol. 9422, 94220X · © 2015 SPIE · CCC code: 0277-786X/15/$18
doi: 10.1117/12.2085948

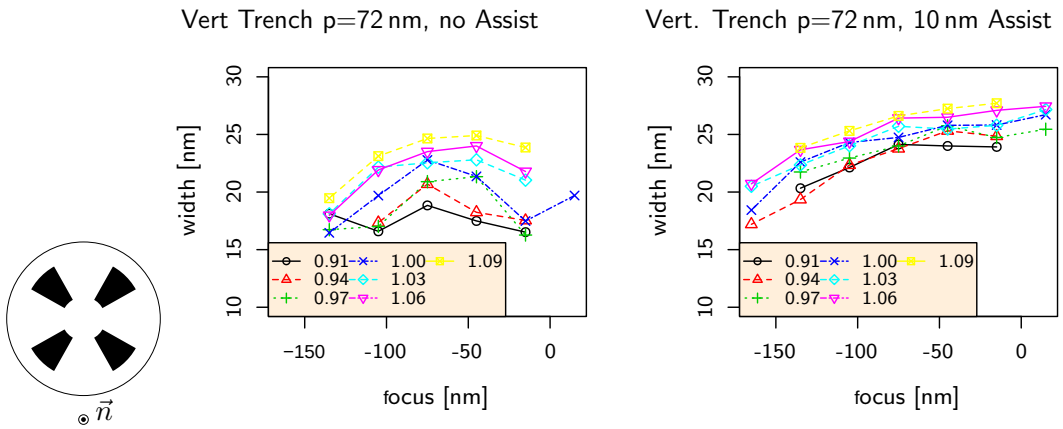

Figure 1. Bossung for trenches printed without (left) and with (right) assist features at 72 nm pitch. The exposures used quasar illumination shown on the left.

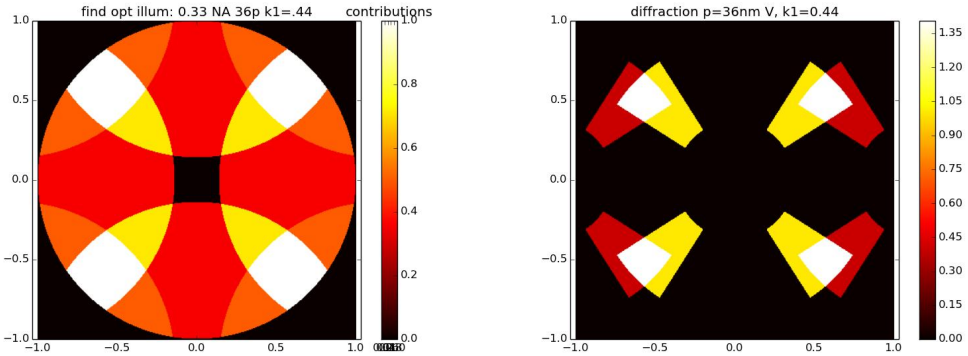

Figure 2. Quasar illumination found by the overlapping circles method (left). the resulting diffraction pattern for 36 nm pitch is shown on the right.

the experiments. The focus shift is not quite the same for horizontal and vertical trenches, but it is very similar as shown in earlier work.[5] Exposures were done using a projection optic of 0.33 NA, and quasar illumination with $\sigma_{\text{out}} = 0.88$ and $\sigma_{\text{in}} = 0.37$. The pattern was formed in 35 nm thick photo resist on top of an under-layer and bare silicon. Patterns were measured using a standard CD scanning electron microscope. The center dose was chosen to print an 18 nm trench at 36 nm pitch approximately to target, and the center focus was chosen to form a maximum width for an isolated trench, which coincided with best focus of the non-assisted case at roughly -75 nm in Fig. 1. Experiments were conducted with two different photo resists, and the results looked substantially similar for both.

The optimized quasar illumination was found by a simple source optimization that used overlapping circles, in the center a circle of radius 1 for the pupil, and 4 more circles of radius 1 around the location of the diffracted orders at 36 nm pitch.[6,7] The areas of maximum overlap, shown on the left in Fig. 2, define the optimum illumination. The areas of the illuminator shown in white and yellow contribute to imaging for both vertical and horizontal lines at 36 nm pitch for the projection optics of 0.33 NA that was used in experiments and simulations. On the right we show the diffraction pattern for the selected illumination for 36 nm pitch. The ideal balance of diffracted orders, where the 1st diffracted order exactly overlaps with the 0th diffracted order at 36 nm pitch is achieved at approximately σ=0.8. The $\sigma_{\text{out}}/\sigma_{\text{in}}$ of 0.88/0.37 chosen is rather low by that measure, but was within the capabilities of our scanner.

In the following sections, we simulate the effect and investigate variables that can modify the best focus shift.

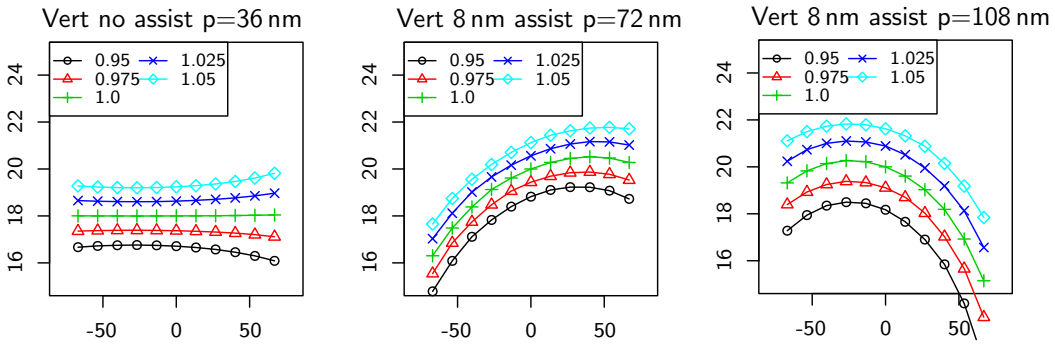

Figure 3. Simulated Bossung curves (linewidth vs focus) for printing vertical trenches at 36, 72, and 108 nm pitch. Target width for 36 nm pitch was 18 for equal lines and spaces, and 20 nm for more relaxed pitches.

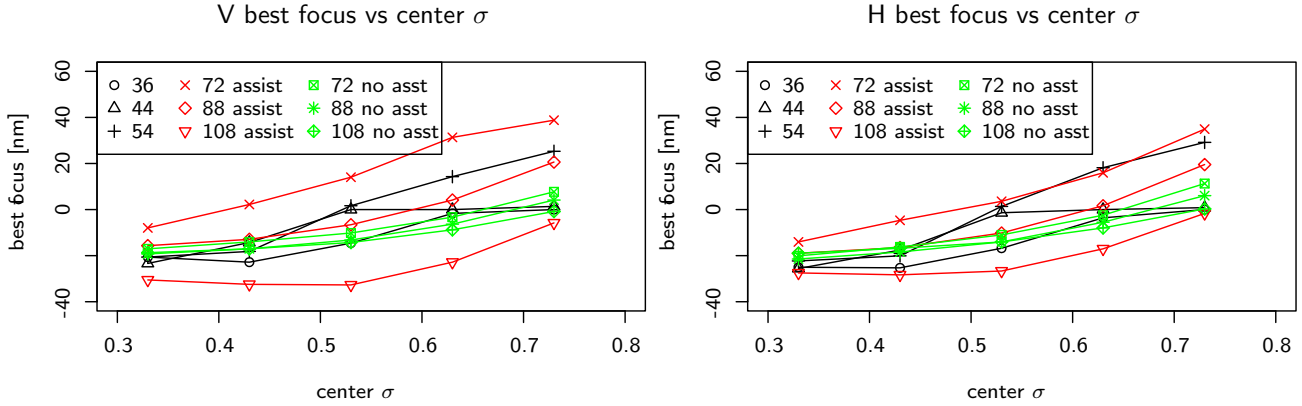

Figure 4. Best focus vs. center σ for vertical (left) and horizontal (right) trenches at various pitches. The difference between outer and inner σ, $\sigma_{\text{out}} - \sigma_{\text{in}}$ is kept constant at 0.5. Best focus is determined in simulation by measuring the center focus of an elliptical fit to the process window.

We then try to explain why this focus shift happens, followed by proposed modifications that may lessen the best focus shift.

2. SIMULATIONS

The simulated Bossung curves for the minimum pitch of 36 nm, as well as the frequently occuring conditions of 2× and 3× minimum pitch are shown in Fig. 3 for vertical trenches. There is no assist feature for the 36 nm case, but a single assist is placed between main features at 72 nm and 108 nm pitch. We observe that not only can we confirm the experimental observation of a positive best focus shift from Fig. 1, but we can also move the best focus to the other extreme at a pitch of 108 nm. We only use a single assist feature for 108 nm pitch intentionally because we would like to investigate this best focus shift effect. At this pitch, it would be possible to place two assist features instead.

All simulations were performed using Panoramic Technology's HyperLith and EM-Suite simulation tools.[8] We used finite-difference time-domain (FDTD) EMF simulations for the mask diffraction calculations, and on the wafer side we used a simple diffused aerial image model with Gaussian FWHM of 15 nm. The mask was a commercially available substrate of 40 bi-layers of Mo/Si, including a capping layer, and a Ta based absorber of dielectric index $n \simeq 0.95$ and absorption of $k \simeq 0.3$.

For our chosen illuminator with $\sigma_{\text{out}}/\sigma_{\text{in}}$ of 0.88/0.37, the center of the pole is roughly at σ=0.63. If we keep the difference $\sigma_{\text{out}} - \sigma_{\text{in}}$ of the illuminator constant at 0.5 and vary the center sigma along the radius we find that the best focus behavior for the various pitches changes with center σ, as shown in Fig. 4. Best focus is

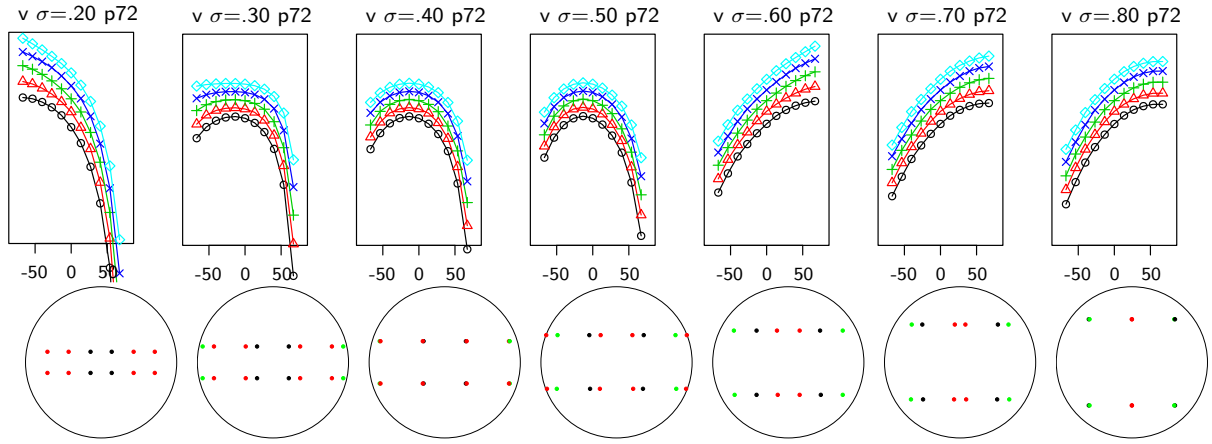

Figure 5. Bossung curves formed by point quadrupoles (top), and corresponding diffraction patterns of the point quadrupoles (bottom). In the diffraction pattern, 0th order is drawn in black, 1st diffracted in red, and 2nd diffracted in green. The center σ radius is varied from 0.2 up to 0.8 in steps of 0.1. For σ going from 0.2 to 0.3 we go from pure 0th and 1st diffracted order to add half the 2nd diffracted order. For σ going from 0.5 to 0.6 we loose half of the 1st diffracted order, which causes the strong Bossung tilt.

determined as the center of an elliptical fit to the process window. In the case of near-isofocal Bossung curves the best focus defaults to 0, which is the case for the dense pitches at large σ settings. Dense features without possibility of assist placement is drawn in black, relaxed pitch with no assist features in green, and relaxed pitch with assist features in red. The best focus for vertical trenches is shown on the left and for horizontal trenches on the right. We observe that there are best focus variations even for the non-assisted case, but that the best focus is much less dependent on pitch than in the assisted case. For our operating point of σ= 0.63, we have best focus for all pitches under investigation within 15 nm for non-assisted trenches, which should not present a big problem in practice. In the case of assist features the best focus varies by roughly 50 nm through pitch. If we simulate Bossung curves using point quadrupole illumination, shown in Fig. 5, we observe a strong dependence of best focus on the σ of the point quasars. The best focus shifts from negative to neutral when half the 2nd diffracted order enters the pupil, and moves very positive when half the 1st diffracted order leaves the pupil. To find out which diffracted orders are collected in the pupil of the projection lens as a function of σ for a pitch p of 72 nm, we calculate the values at which the diffracted orders leave or enter the pupil. Half of the 1st diffracted leaves the pupil when σ fulfills the condition

$$\sqrt{\left(\frac{\lambda}{p\,\mathrm{NA}}+\frac{\sigma}{\sqrt{2}}\right)^2+\frac{\sigma^2}{2}}>1\ ,$$

while half of the 2nd diffracted order enters the pupil when σ fulfills the condition

$$\sqrt{\left(\frac{2\,\lambda}{p\,\mathrm{NA}}-\frac{\sigma}{\sqrt{2}}\right)^2+\frac{\sigma^2}{2}}<1\ .$$

For σ varying from 0 to 1, we can plot the fraction of diffracted orders that are in the projection pupil at 72 nm pitch, as shown in Fig. 6. The 0th order is drawn in black, and is always fully captured in the pupil, independent of σ. The $\pm$1st diffracted orders, drawn in red, are fully in the pupil up to a σ of a little more than 0.6. The $\pm$2nd diffracted orders, drawn in green, enter the pupil a little above a σ of 0.2. The upper and lower bounds of the quasar illuminator are drawn in black dotted lines, indicating which σ range the illuminator covers. On the right in Fig. 6 we show the simulated best focus for quadrupole illumination in the non-assisted case in black and cyan for vertical and horizontal trenches at 72 nm pitch. It turns out that the best focus varies also in the non-assisted case, but the variations are not as strong as in the assisted case, here drawn in red and magenta for vertical and horizontal trenches. The assist features in the simulations were 8 nm wide in wafer dimensions.

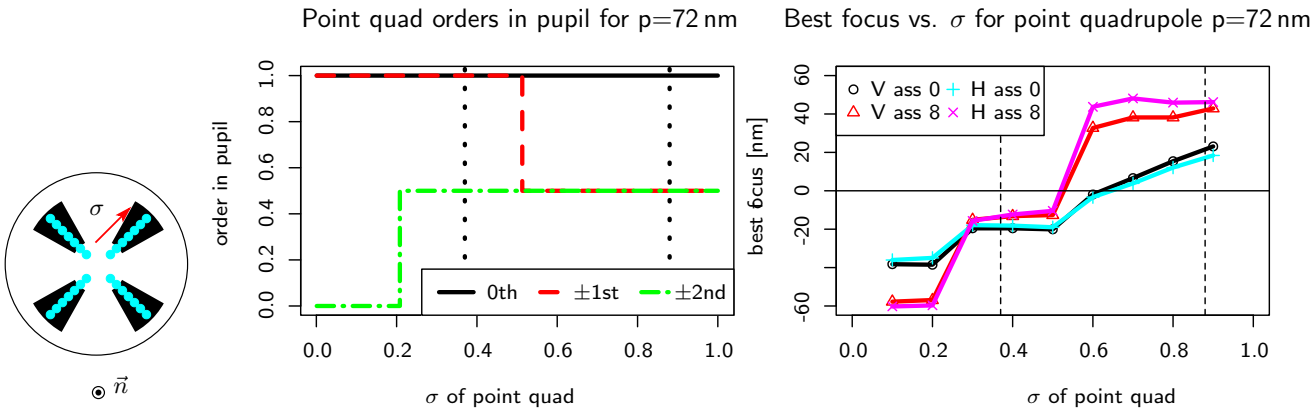

Figure 6. The left inset shows the variation of quadrupole σ from 0.2 to 0.8 in cyan dots. In the center, the fraction of 0th, ±1st, and ±2nd diffracted orders in the pupil of the projection optics is shown for 72 nm pitch. The inner and outer σ of the quasar illuminator is indicated by the dotted black lines. On the right, we show the simulated best focus for a point quadrupole illumination vs σ for non-assisted case (black and cyan) and the assisted case for 8 nm assist features in red and magenta for vertical and horizontal trenches, respectively.

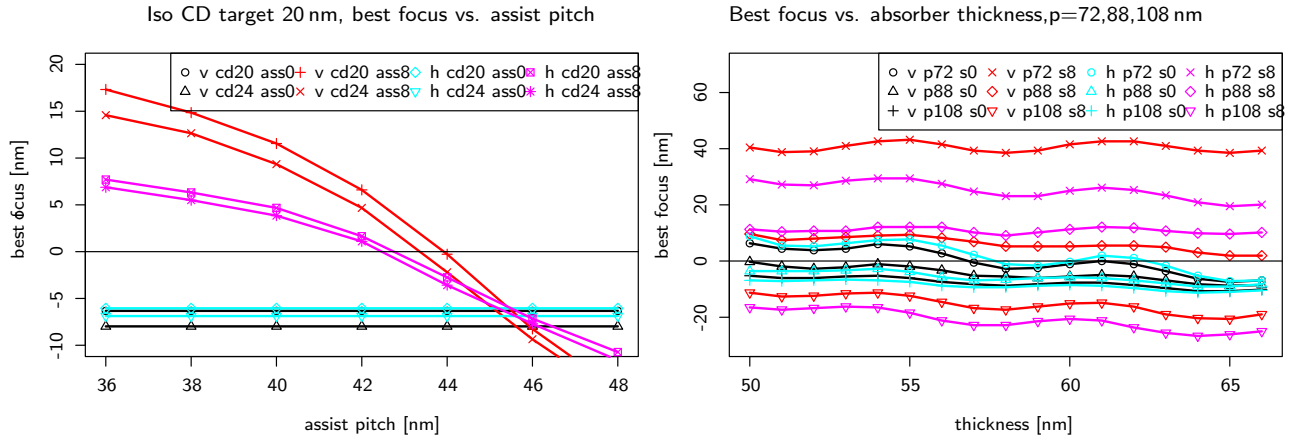

Figure 7. Left: best focus variation vs assist pitch. Curves are slightly different for a mask dimension of 20 nm vs 24 nm, with the dose adjusted to print as 20 nm. For the chosen illuminator we require an assist pitch of 46 nm for the assisted trench to have the same best focus as a non-assisted trench. Right: Best focus variations for 72, 88, and 108 nm pitch with a single assist feature between main features, and for the non-assisted case. If there are no assist features the thickness can be tuned within limits to reduce best focus shifts, with assist features the tuning range is very limited.

Because the best focus shift depends not only on the complex diffraction coefficient due to thick mask effects but also on the diffracted orders that are collected in the pupil we investigate next the dependence of best focus on assist feature pitch, for the case of isolated trenches. The simulated results are shown on the left side in Fig. 7. In this plot of best focus vs. assist feature pitch for a single assist on either side of the main feature, we plot two trench sizes, 20 and 24 nm, with the dose adjusted to print isolated 20 nm trenches. For the chosen illuminator we require an assist feature pitch of 46 nm for the assisted trench to have the same best focus as a non-assisted trench. This knob is so effective that a variation of assist pitch is probably the best and easiest way to control pattern dependent best focus variations where we have the liberty to vary the assist pitch.

On the right side of Fig. 7, we are simulating the impact of absorber thickness on best focus. Dependence of best focus on absorber thickness has been investigated both in EUV and ArF lithography before[9,10] in order to optimize the absorber thickness on the mask. We vary the absorber thickness around our mask absorber thickness of 58 nm to see if this is an easy way to improve the defocus variations. It turns out that we can use absorber thickness as a knob to adjust best focus for the non-assisted case, drawn in black for vertical and

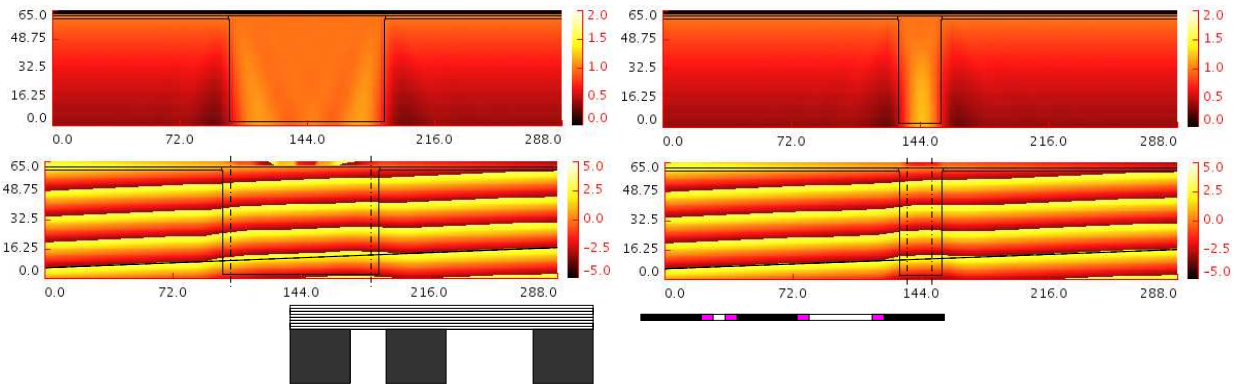

Figure 8. Field magnitude and phase for incident light without any reflection off the multi layer substrate which have been replaced with vacuum for the simulations. On the left, we show a main feature of 88 nm size in mask dimensions (22 nm wafer dimensions), on the right an assist feature of 32 nm size in mask dimensions. There is a gradual transition of the phase from vacuum into the absorber, and on either side of the interface the phase is modified, advanced in the vacuum and retarded in the absorber. On the bottom right we show the equivalent thin mask that can conceptually be used for simulations instead of full EMF simulations.

cyan for horizontal trenches. If we add assist features of 8 nm width there is still some variation of best focus with absorber thickness, but no significant trend one way or the other. Absorber thickness optimization may modify some other lithographic properties and phase shifting behavior, but appears incapable to modify feature dependent best focus variations.

3. DISCUSSION

3.1 Complex Diffraction Coefficient

As an explanation for the phase effect, we follow Erdmann et al.[11] and calculate the field in the absorber and vacuum with the multilayer mirror removed, so only light incident from the top is involved. We observe that the calculated fields in close proximity to the absorber and inside the absorber are influenced by the interface, as shown in Fig. 8. The lower index of refraction in the absorber material advances the phase in the absorber and in close proximity relative to the vacuum, while it retards the phase inside the absorber in close proximity to the vacuum relative to the bulk absorber. On the left side, we show a large opening of 88 nm size in mask dimensions (4×), and on the right side we show a small opening of 32 nm size (4×), representative of assist features. On the bottom of Fig. 8, we show a conceptual equivalent thin mask on the right, which would replace a thick mask drawn on the left. The magenta regions indicate a phase shifted region adjacent to the absorber. This approach has been used before in ArF masks[12] and is also used in optical proximity correction software where exact calculation of the diffraction patterns would be too expensive computationally.[13]

3.2 Waveguide Effect

Because the absorber in our simulations has a real part of the refractive index of 0.953 which is smaller than 1, the vacuum turns out to be the optically denser material. This means that we can have total internal reflection of light in vacuum at the vacuum/absorber interface. The maximum incident angle that causes total internal reflection is $\arcsin(0.953) = 72.55^o$. With the chief ray angle of illumination at 6^o and a mask side NA of 0.0825, the maximum angle of incidence normal to the mask at σ=1 is roughly 10.7^o. This means that for vertical sidewalls of the absorber we have a minimum angle of incidence of 79.3^o. Thus we have total internal reflection and negligible coupling of light into the absorber. This is the reason why for a small aperture we can still have high transmission of light as we would have in a waveguide. If the index of the absorber is further reduced, one can have total internal reflection at even larger angles of incidence, so that one can have good transmission through very small apertures even at angles that would be needed for very high NA projection systems, as shown in earlier work.[14] The transmitted light through the absorber opening, after removing the multilayer mirror underneath the absorber, is shown in Fig. 9. On the top, we show the transmission through a 88 nm opening

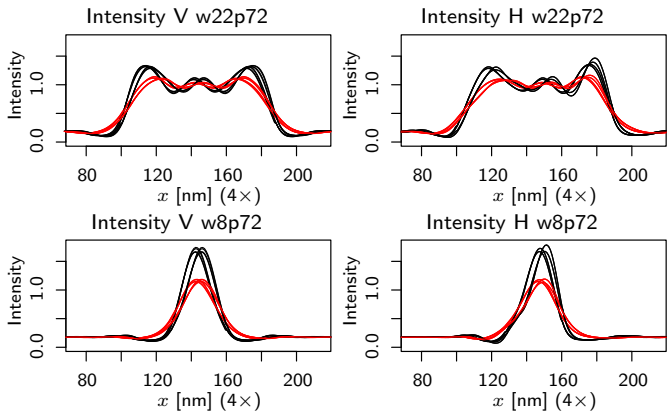

Figure 9. Waveguide effect: plot of single pass transmission of light through the absorber opening into the multi-layer base of the mask. The multi layer is removed for this simulation, so no reflection is considered. On the top, we have the vertical and horizontal intensity transmission of a 88 nm (4×) opening on the mask approximating the main feature, on the bottom a 32 nm (4×) opening on the mask approximating an assist feature. In black, we show the transmission through the absorber for the four poles and two polarizations each with the regular real part of the index of refraction n, and in red we show the transmission for a fictional material of index 1, which would be index matched to vacuum.

at 288 nm pitch (4× dimensions), which is similar in size to a main feature on the mask, and on the bottom we show the transmission through a 32 nm opening at 288 nm pitch (4× dimensions), which is similar in size to an assist feature. In black, we draw the results for the absorber that was used in experiment and simulations, with n=0.953 and k=0.031, and in red we draw results with a fictional absorber of n=1.0 and k=0.031, matching the absorber with vacuum in the real part of the index of refraction. For each color there are eight graphs, one each for the four poles and two each for incident TE and TM polarization. There is a very small split in curves for the two polarizations, and another split for the different incidence angles for vertical lines, and a larger difference for the angle of incidence, which for vertical lines is symmetrical and for horizontal lines is further split. The most interesting feature though is that for the non-matched index case of n=0.953, we have a much stronger ringing behavior than for the matched case of n=1.0. This is partially due to the fact that for the matched case light can bleed into the absorber and get attenuated, while in the non-matched case we have total internal reflection in the vacuum. In particular for the assist feature size absorber opening we have a much higher intensity for the non-matched case compared to the matched absorber case. This means that the assist feature size has to be increased if the absorber index is closer matched to the index of vacuum.

3.3 Diffracted Orders and Defocus

The complex diffraction coefficient that is caused by the thick mask effects is a necessary condition for best focus shift. In addition to this, the location of the diffracted orders in the pupil cause a different focus behavior, depending on which orders are captured. Figure 10 shows on the left side the quasar illumination used in experiments and simulations, and we wish to investigate the green, cyan, and red points on the lower right quasar illumination element. The red and cyan points are at a σ location above 0.6, which have a very positive best focus, as shown in Fig. 6, while the green point has both ±1st diffracted orders in the pupil. Moving on to the center of Fig. 10, we draw the diffracted orders as they fall into the pupil on the top. On the bottom, we indicate the defocus term that is picked up for each of the diffracted orders, and which can be approximated with the parabolic Zernike term Z_4 with origin in the center of the pupil. Each diffracted order picks up such a phase term commensurate with it's location in the projection pupil. If we draw the diffraction coefficient of a trench at 72 nm pitch with assist features, as shown on the right in Fig. 10, then the defocus rotates each of the diffraction orders in the phasor diagram as indicated conceptually by the curved arrows. This is an example for a TE incident wave diffracting into a TE reflected wave, but not only are there TM incident waves, but there are also cross scattering elements, and also all the other illuminator elements from all four quadrupoles to consider for a complete treatment.

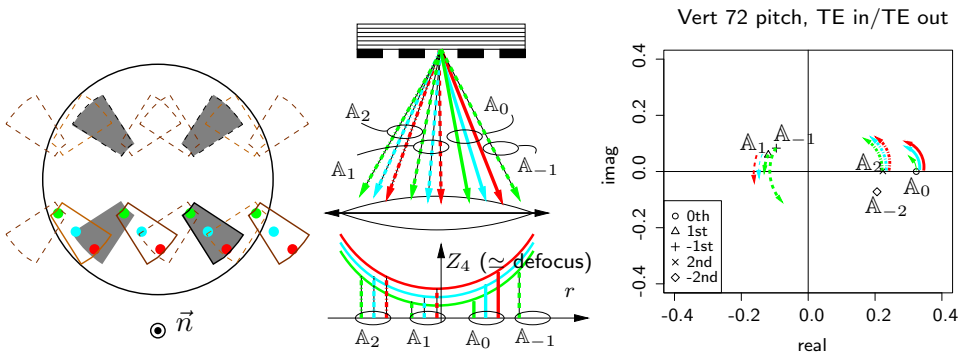

Figure 10. Diffraction pattern for 72 nm pitch case, we select three points (red, cyan, green from outer to inner) in the lower right pole of the quasar (left). Diffracted orders of each of the parts of the illuminator land in different radial distances from the pupil origin and picks up a defocus term (center). Each complex diffraction coefficient rotates according to the defocus at the pupil location.

For pitches that only use up to the 2nd diffracted orders, each part of the illuminator element generates a field $\mathbb{U}$ in the wafer plane

$$\begin{aligned}\mathbb{U}(x,y,z) &= \mathbb{A}_0 e^{ik(\xi_0 x+\eta_0 y+\zeta_0 z)} + \mathbb{A}_1 e^{ik(\xi_1 x+\eta_1 y+\zeta_1 z)} + \mathbb{A}_{-1} e^{ik(\xi_{-1} x+\eta_{-1} y+\zeta_{-1} z)} \\ &+ \mathbb{A}_2 e^{ik(\xi_2 x+\eta_2 y+\zeta_2 z)} + \mathbb{A}_{-2} e^{ik(\xi_{-2} x+\eta_{-2} y+\zeta_{-2} z)} \quad ,\end{aligned}$$

where the $\mathbb{A}_n$ are the complex diffraction coefficients. For the cyan and red points in Fig. 10, we have $\mathbb{A}_{-1} = \mathbb{A}_{-2} = 0$, while for the green point we have only $\mathbb{A}_{-2} = 0$. If we have a phase of ϕ_n due to defocus for each of the diffraction coefficients, set $\mathbb{A}_{-2} = 0$, observe the field at $z = 0$ and look only at vertical gratings at $y = 0$ we have

$$\mathbb{U}(x) = \mathbb{A}_0 e^{i(k\xi_0 x+\phi_0)} + \mathbb{A}_1 e^{i(k\xi_1 x+\phi_1)} + \mathbb{A}_2 e^{(ik\xi_2 x+\phi_2)} + \mathbb{A}_{-1} e^{i(k\xi_{-1} x+\phi_{-1})} \quad .$$

The intensity in the wafer plane due to such a field is

$$\begin{aligned}I(x) &= \mathbb{U}(x)\mathbb{U}^*(x) \\ &= A_0^2 + A_1^2 + A_2^2 + A_{-1}^2 && (1)\\ &+ \mathbb{A}_0\mathbb{A}_1^* e^{ik(\xi_0-\xi_1)x+i(\phi_0-\phi_1)} + \mathbb{A}_1\mathbb{A}_0^* e^{-ik(\xi_0-\xi_1)x-i(\phi_0-\phi_1)} && (2)\\ &+ \mathbb{A}_1\mathbb{A}_2^* e^{ik(\xi_1-\xi_2)x+i(\phi_1-\phi_2)} + \mathbb{A}_2\mathbb{A}_1^* e^{-ik(\xi_1-\xi_2)x-i(\phi_1-\phi_2)} && (3)\\ &+ \mathbb{A}_0\mathbb{A}_2^* e^{ik(\xi_0-\xi_2)x+i(\phi_0-\phi_2)} + \mathbb{A}_2\mathbb{A}_0^* e^{-ik(\xi_0-\xi_2)x-i(\phi_0-\phi_2)} && (4)\\ &+ \mathbb{A}_{-1}\mathbb{A}_0^* e^{ik(\xi_{-1}-\xi_0)x+i(\phi_{-1}-\phi_0)} + \mathbb{A}_0\mathbb{A}_{-1}^* e^{-ik(\xi_{-1}-\xi_0)x-i(\phi_{-1}-\phi_0)} && (5)\\ &+ \mathbb{A}_{-1}\mathbb{A}_1^* e^{ik(\xi_{-1}-\xi_1)x+i(\phi_{-1}-\phi_1)} + \mathbb{A}_1\mathbb{A}_{-1}^* e^{-ik(\xi_{-1}-\xi_1)x-i(\phi_{-1}-\phi_1)} && (6)\\ &+ \mathbb{A}_{-1}\mathbb{A}_2^* e^{ik(\xi_{-1}-\xi_2)x+i(\phi_{-1}-\phi_2)} + \mathbb{A}_2\mathbb{A}_{-1}^* e^{-ik(\xi_{-1}-\xi_2)x-i(\phi_{-1}-\phi_2)} && (7)\end{aligned}$$

Line 1 is a DC value, lines 2, 3, and 5 contribute to a pitch of p_0, which is 72 nm in our example. Lines 4 and 6 are at a pitch of $p_0/2$, which is 36 nm in this case, and line 7 contributes at pitch $p_0/3$, which is 24 nm here. As mentioned before, $\mathbb{A}_{-1} = 0$ for the red and cyan points, so the last term in line 1 disappears, as well as lines 5, 6, and 7.

If we assume that the magnitude A_n and phase α_n of the diffraction orders $\mathbb{A}_n$ is independent of the location within the illumination element (i.e. $\mathbb{A}_n$ are shift invariant for the green, cyan, and red elements) we can write for the cyan and red points

$$\begin{aligned}I_{c,r}(x) &= A_0^2 + A_1^2 + A_2^2 + A_0 A_1 \cos(2\pi\frac{x}{p_0} + \Delta\alpha_{0,1} + \Delta\phi_{0,1c,r}) \quad (8)\\ &+ A_1 A_2 \cos(2\pi\frac{x}{p_0} + \Delta\alpha_{1,2} + \Delta\phi_{1,2c,r}) + A_0 A_2 \cos(2\pi\frac{2x}{p_0} + \Delta\alpha_{0,2} + \Delta\phi_{0,2c,r}) \ ,\end{aligned}$$

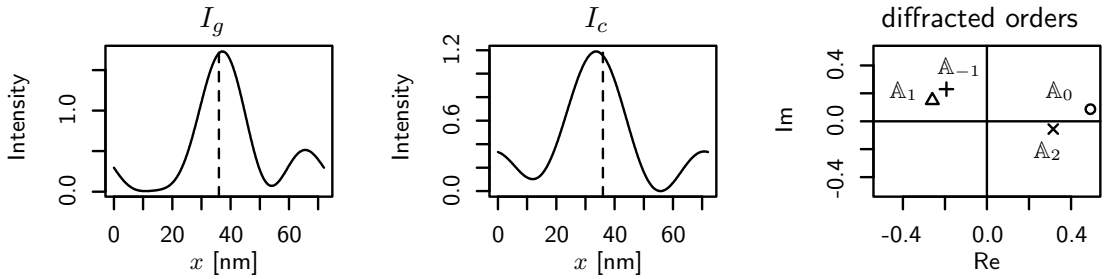

Figure 11. Image calculation of adjacent points in the illuminator with characteristic set of diffraction coefficients. One image, I_g, assumes four diffracted orders, I_c assumes three diffracted orders. No defocus was assumed.

and for the green point

$$\begin{aligned} I_g(x) &= A_0^2 + A_1^2 + A_2^2 + A_{-1}^2 + A_0 A_1 \cos(2\pi\frac{x}{p_0} + \Delta\alpha_{0,1} + \Delta\phi_{0,1g}) \\ &+ A_1 A_2 \cos(2\pi\frac{x}{p_0} + \Delta\alpha_{1,2} + \Delta\phi_{1,2g}) + A_{-1} A_0 \cos(2\pi\frac{x}{p_0} + \Delta\alpha_{-1,0} + \Delta\phi_{-1,0g}) \\ &+ A_{-1} A_1 \cos(2\pi\frac{2x}{p_0} + \Delta\alpha_{-1,1} + \Delta\phi_{-1,1g}) + A_0 A_2 \cos(2\pi\frac{2x}{p_0} + \Delta\alpha_{2,0} + \Delta\phi_{2,0g}) \\ &+ A_{-1} A_2 \cos(2\pi\frac{3x}{p_0} + \Delta\alpha_{-1,2} + \Delta\phi_{-1,2g}) \quad . \end{aligned} \tag{9}$$

Here, the $\Delta\alpha_{m,n}$ are the difference in phase angle of the respective diffractive orders, and the $\Delta\phi_{m,n}$ are the differences in focus between the diffracted orders for the respective illumination element, which are different dependent on where in the pupil the diffracted order ends up. We have also used $k(\xi_{0,1,2} - \xi_{-1,0,1}) = 2\pi\frac{x}{p_0}$, $k(\xi_{1,2} - \xi_{-1,0}) = 2\pi\frac{2x}{p_0}$, and $k(\xi_2 - \xi_{-1}) = 2\pi\frac{3x}{p_0}$. The pitch p_0 in our case is 72 nm, and the diffracted orders are drawn to that effect in Fig. 10. So the cyan and red illuminator elements have image contributions at p_0 and $2p_0$, while the green illuminator element has an additional component at $3p_0$, and more imaging components at p_0 and $2p_0$ because of the added -1st diffracted order. For each of the monopole illuminators that make up the intensities calculated in Eqns. 8 and 9, we observe that it contains only a constant offset and various cosine terms. The cosine terms create an image for the various diffracted order combinations and contribute to contrast, where the maximum contrast determines best focus. For each such contribution the cosine terms are maximized for $\Delta\alpha_{m,n} + \Delta\phi_{m,n} = l\pi$, where m and n are indices of various diffracted orders, and l is an integer including 0. Looking back at the phasor diagram on the right of Fig. 10, we can state that the contrast is highest for an image contribution if the rotated diffraction coefficients in the phasor plot are 0^o or 180^o from each other, which may happen at a focus position that is determined by the initial relative phase angle. And depending on the σ of an illumination element, there may be three or four diffracted orders captured, which strongly influences the final image.

If we were to move a monopole illuminator from the green towards the cyan position, for the transition where the 2nd diffracted order leaves the pupil one can imagine a very small $\Delta\sigma$ over which the complex diffraction coefficient can surely be assumed constant. If we plot the images for green and cyan images according to Eqns. 9 and 8, as shown in Fig. 11, we can see that the image for that is produced for the diffraction orders shown on the right is very different for the green point I_g on the left and the cyan point I_c in the center. We assumed some fictional but characteristic diffraction coefficient, with $\mathbb{A}_0 = 0.5\angle 10$, $\mathbb{A}_1 = 0.3\angle -30$, $\mathbb{A}_{-1} = 0.3\angle -50$, and $\mathbb{A}_2 = 0.32\angle -10$. The character of the image changes dramatically with a very small change in σ value, which is due to the fact that for I_g we have four diffracted orders for imaging, while we have only three orders for I_r. The asymmetries that are observed are to the most part compensated for the monopole on the other side of the illuminator when we use quadrupole illumination.

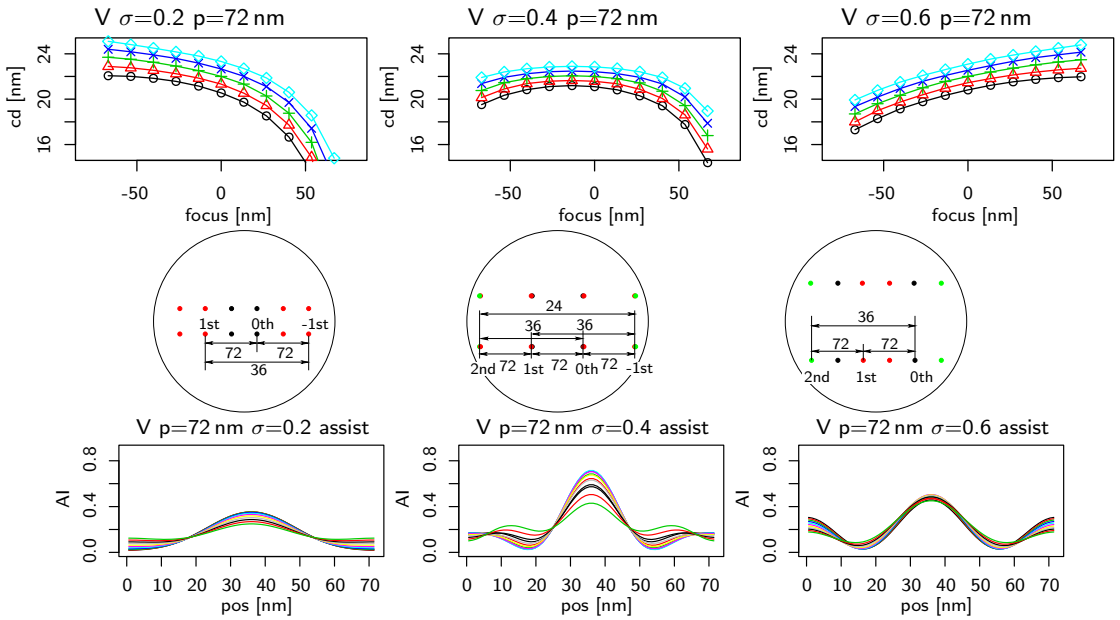

Figure 12. Bossung plots for point quadrupole illumination (top), diffracted orders in pupil and associated pitches (center), and resulting aerial image through focus for the point quasar with σ of 0.2, 0.4, and 0.6. In the diffracted orders, each captured order can interfere with another one from the same source point. For the right bottom source point of the point quasar we have annotated the resulting pitches for our case of 72 nm pitch with assist features. In the aerial image on the bottom, we can observe that the case of 0.4 σ provides the best image because four diffraction orders are captured, so the image is modulated with 24 nm pitch components.

Going back to the point quadrupole illumination that we discussed in Figs. 5 and 6, we understand better the resulting image. The Bossungs for the point quadrupoles of σ=0.2, 0.4, and 0.6 are shown in the top of Fig. 12, in the middle we show the diffracted orders, and on the bottom the aerial images through focus. In the plot of diffracted orders, we annotated the interfering orders that form the image in the pupil, using as an example the right bottom illuminator element. For the case of 0.2 and 0.6 σ, we have only three diffracted orders in the pupil and only pitches of 72 nm and 36 nm can contribute to imaging, leading to a poor aerial image, and large focus shift. For the case of 0.4 σ, we have a much better aerial image because we also have interference at 24 nm pitch, in addition to larger contributions at 36 and 72 nm pitch, while showing only a moderate focus shift.

3.4 Contrast Degradation through Image Shift

For the aerial images shown in Fig. 11, we observe a center shift from I_g to I_c relative to the center position drawn by the dashed lines. More importantly, this center position can change depending on σ. This shift can in most cases be compensated through the illumination element on the opposite side of the illuminator. In Fig. 13, we plot through focus aerial images for trenches printing at 72 nm pitch with monopole illumination of $\sigma = 0.8$ on the quadrupole axis for both a regular absorber with n=0.953, as well as a fictional absorber with the same absorption value k, but an index n=1 that has been matched to vacuum. Each pole's family of curves for the various focus values is drawn in a different color, on one side we have the black and blue curves for two of the poles, on the other side the green and red curves – because of the large number of defocus values and overlap we see mainly blue and green. The first plot shows the case for vertical trenches. The green and blue curves are for the monopoles that lie closest to the normal incidence on the mask, so their peak intensity is largest. The green and red poles' image is shifted to the left, the black and blue is shifted to the right. The second plot shows the same case for horizontal trenches, and here the black/blue and green/red curves are identical. The intensity mismatch between left and right peaks is very pronounced, however. This is because the transmission through the absorber and reflection off the multilayer mirror becomes less efficient the farther the light is incident from the normal. In both cases, the image contrast is reduced through averaging the shifted images, and in the case of

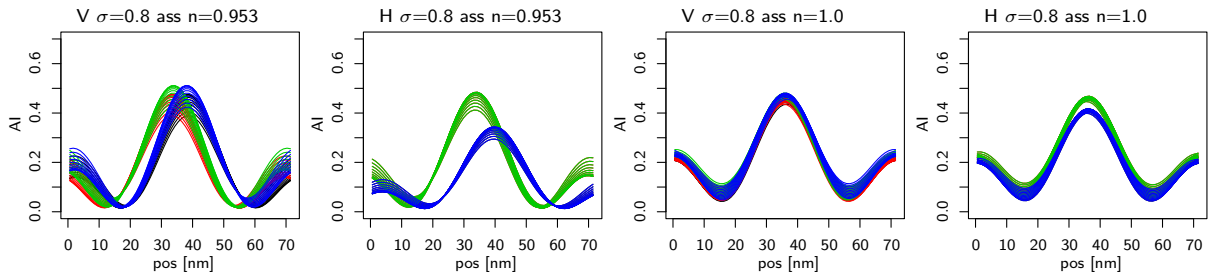

Figure 13. Contrast degradation through aerial image position shift. We plot aerial image through focus for each of the four monopoles in one graph. The black and blue curves are for two of the poles of the point quadrupole, green and red are for the other two poles. All plots are for $\sigma = 0.8$ monopoles printing trenches at 72 nm pitch with assist features, the first one for vertical trenches, the second for horizontal trenches, the third and fourth for vertical and horizontal trenches assuming a fictional absorber material with the same k of 0.031 and an n of 1.0, matching the vacuum dielectric constant.

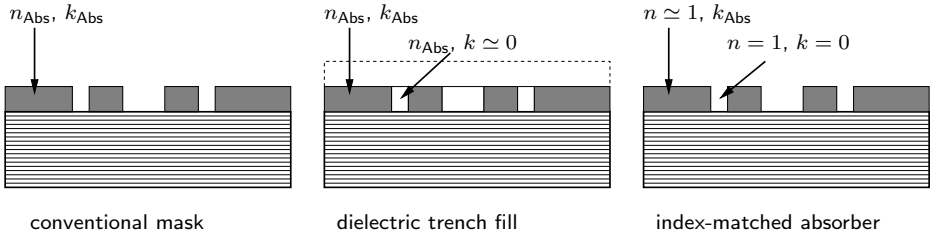

Figure 14. Possible solutions to the focus shift problem: cover the gaps in the absorber with an index matched material (center), or choose a material that is index matched to vacuum (right).

horizontal trenches we also expect a net image shift towards the stronger intensities. The third and fourth graphs show the same plots for the fictional material with the real part of the index of refraction matched to vacuum. There is still a residual image shift visible, but it is much reduced compared to the non-matched material. It is of course still possible to have complex diffraction coefficients in the reflected light because we are dealing with a thick mask, but the matching of the absorber prevents a strong deviation from the ideal case of no image shift. The placement shift of horizontal patterns and vertical patterns away from the field center is well known in EUV lithography and needs to be considered for source optimization.[15]

3.5 Possible Fixes

Since the main reason for the best focus shift is the phase term that is picked up by the light traveling adjacent to the absorber with the real part of the index of refraction different from vacuum, this effect can be fixed by changing the absorber material or filling in the trenches on the mask. The two possible solutions are shown in Fig. 14. In the center, we show a solution involving filling in the mask trenches with a material that is mostly transparent and whose index of refraction is matched to that of the absorber. If we use Henke's tabulated data from the LBNL web site as reference,[16] we can, for example, use an absorber of TaN and fill in the gap with molybdenum, which is much more transparent, yet almost exactly matched to TaN. If it was possible to use copper as an absorber, one could fill the gap with carbon or $MoSi_2$, which is a good match. In the case of the gap fill it is also possible to overfill the trenches to have a planar surface with the absorber covered as well. The other method, on the right, is to match the absorber to vacuum itself. There are several materials that have an index close to unity, for example aluminum, germanium, or magnesium, or tellurium. All but the last have absorption less than the tantalum based absorbers, so a taller absorber stack would be needed, exacerbating the shadowing effect in EUV. These are suggestions based only on the tabulated values of n and k at EUV wavelengths and are not statements on practical implementation. In practice, the material needs to be safe and easy to etch, while also providing for sufficient contrast during mask inspection. Recently, SnTe and ZnTe have been suggested, which have an index much closer to unity than the Ta based absorbers while providing significantly higher absorption.[17] A thinner absorber with index close to unity may then improve on the phase shift along the vacuum/absorber interface, while simultaneously reducing the shadowing effect due to non-normal incidence of the chief ray.

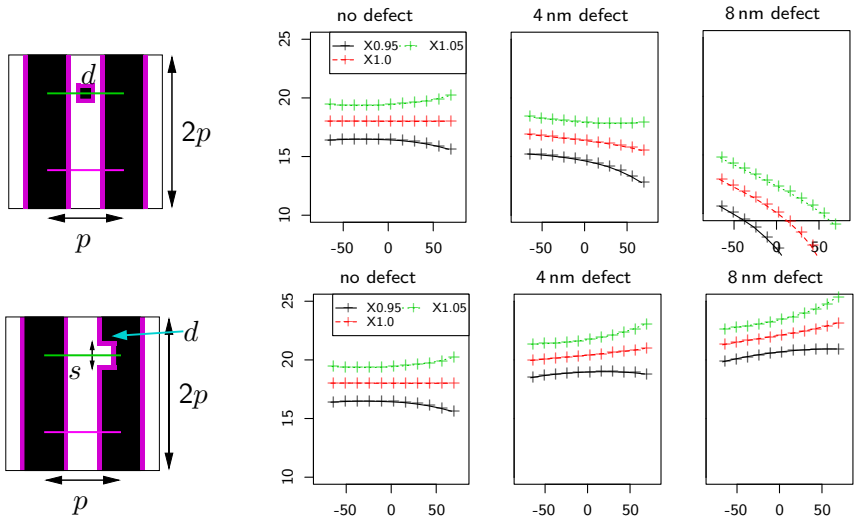

Figure 15. Printing of an opaque defect (top) and a mousebite defect (bottom), and associated Bossung curves for the trench at the defect location indicated in green. In both cases, the additional phase area close to the absorber, indicated in magenta, is increased, leading to nominally opaque defects to print like phase defects would print.

3.6 Defects

One interesting aspect of the phase advance of the light that is travelling close to the absorber edge is that an increase of absorber edge can lead to phase effects in printing. Such a situation is shown in Fig. 15, where we show a programmed defect in the center between absorbers on the top and a mouse bite defect on the bottom. The left shows in black the absorber that is simulated, and in magenta we draw the region close to the absorber, where the phase advance occurs. The pitch that is modeled here is 36 nm in wafer coordinates, and the simulation domain on the mask was twice the pitch in both x and y. The opaque defect on the top was a square of size d, and the Bossung curves were measured along the green metrology section, while the exposure was set to print on target in the magenta metrology section. On the right, we show Bossung curves for the trench printing with no defect, 4 nm size defect, and 8 nm size defect. The Bossung plots are strongly tilted, which is the characteristic of a phase defect which could ordinarily be blamed on a multi layer defect in the mask. In this case, however, it is a nominally opaque defect that acts like a phase defect in printing. This is because of the increased area in proximity to the absorber/vacuum interface. Equally, the mousebite defect is defined as a 10 nm long section s which moves into the absorber by a distance d. The measurement is again done at the green section. First, we show the Bossung with no defect, which is nice and iso-focal. Once the mousebite moves into the absorber, the total circumference around the absorber is increased, and we see an apparent phase type defect which is not caused by any multilayer defect underneath the absorber.

4. CONCLUSIONS

We investigated the best focus shift that is present in EUV masks. There are two important factors that contribute to the shift in best focus in EUV imaging. First, the dimensions of the mask are large both in lateral dimension and in thickness compared to the wavelength of the light. This leads to thick mask effects in the form of complex diffraction coefficients. The physical reason for this is the light traveling in proximity to the absorber/vacuum interface advancing in phase relative to the light that is not in proximity to the absorber. The effect that these complex diffracted orders have on focus strongly depends on the shape of the illuminator. Each illumination direction has it's own characteristics, depending on how many and which diffracted orders are collected in the pupil of the projection lens. A small change in σ can have a dramatic effect in best focus.

We investigated influence on absorber thickness and assist feature placement on best focus and found that while absorber thickness is not a good variable to tune best focus effects, assist feature placement can have a strong effect on best focus. In particular for patterns where we have freedom to place assist features, such as

isolated patterns, we can dial in the best focus over a large range. We also proposed possible solutions to reduce thick mask effects, such as matching the absorber index to that of the transmissive region, by either filling the gaps between absorbers with a matched dielectric, or by choosing an absorber with index close to unity.

Finally, we investigated the lithographic effect of programmed defects on imaging. Programmed defects, which have identical n and k values to the rest of the absorber, can act like phase defects because of the absorber/vacuum mismatch of dielectric constants. The Bossung curves of both opaque defects in clear regions and mousebite defects in opaque regions can have tilted Bossung curves, which could otherwise be associated with defects in the multilayers underneath the absorber.

Acknowledgments

This work was performed by the research and development alliance teams at various IBM research and development facilities. We would like to thank the Ken Goldberg and Antoine Wojdyla of the LBNL SHARP tool for measurements. We would also like to thank Tim Brunner, Todd Bailey, and Matt Colburn for discussions.

REFERENCES

[1] Krautschik, C. G., Ito, M., Nishiyama, I., and Otaki, K., "Impact of the EUV mask phase response on the asymmetry of Bossung curves as predicted by rigorous EUV mask simulations," *Proc. SPIE* **4343**, 392–401 (2001).

[2] Yan, P.-Y., "Understanding Bossung curve asymmetry and focus shift effect in EUV lithography," *Proc. SPIE* **4562**, 279–287 (2002).

[3] Yan, P.-Y., "Dark field EUVL mask for 45nm technology node poly layer printing," *Proc. SPIE* **4889**, 1106–1112 (2002).

[4] Rizvi, S., ed., [*Handbook of Photomask Manufacturing Technology*], ch. Masks for Extreme Ultraviolet Lithography, 263–264, CRC Press (2005). http://dx.doi.org/10.1201/9781420028782.

[5] Burkhardt, M., McIntyre, G., Schlief, R., and Sun, L., "Clear sub-resolution assist features for EUV," *Extreme Ultraviolet (EUV) Lithography V* **9048**, 904838–904838–7, SPIE (2014).

[6] Burkhardt, M., Yen, A., Progler, C., and Wells, G., "Illuminator design for the printing of regular contact patterns," *Microelectron. Eng.* **41-42**, 91–95 (1998).

[7] Granik, Y., "Source optimization for image fidelity and throughput," *Journal of Microlithography, Microfabrication, and Microsystems* **3**(4), 509–522 (2004).

[8] Panoramic Technology, http://www.panoramictech.com.

[9] Davydova, N., de Kruif, R., Rolff, H., Connolly, B., van Setten, E., Lammers, A., Oorschot, D., Fukugami, N., and Kodera, Y., "Experimental approach to euv imaging enhancement by mask absorber height optimization," *Proc. SPIE* **8886**, 88860A–88860A–15 (2013).

[10] Bouma, A., Miyazaki, J., van Veen, M., and Finders, J., "Impact of mask absorber and quartz over-etch on mask 3d induced best focus shifts," *Proc. SPIE* **9231**, 92310S–92310S–9 (2014).

[11] Erdmann, A., Evanschitzky, P., and Fühner, T., "Mask diffraction analysis and optimization for extreme ultraviolet masks," *Journal of Micro/Nanolithography, MEMS, and MOEMS* **9**(1), 013005–013005–8 (2010).

[12] Tirapu-Azpiroz, J., Burchard, P., and Yablonovitch, E., "Boundary layer model to account for thick mask effects in photolithography," *Proc. SPIE* **5040**, 1611–1619 (2003).

[13] Lam, M., Adam, K., and Neureuther, A. R., "Domain decomposition methods for simulation of printing and inspection of phase defects," *Proc. SPIE* **5040**, 1492–1501 (2003).

[14] Yeung, M. and Barouch, E., "The feasibility of EUV lithography for printing circuits with 4 nm feature size," *Proc. SPIE* **9235**, 923514–923514–9, SPIE (2014).

[15] Liu, X., Howell, R., Hsu, S., Yang, K., Gronlund, K., Driessen, F., Liu, H.-Y., Hansen, S., van Ingen Schenau, K., Hollink, T., van Adrichem, P., Troost, K., Zimmermann, J., Schumann, O., Hennerkes, C., and Grupner, P., "Euv source-mask optimization for 7nm node and beyond," *Proc. SPIE* **9048**, 90480Q–90480Q–11 (2014).

[16] Henke, B. Web Site. http://henke.lbl.gov/optical_constants/getdb2.html.

[17] Park, S., Peranantham, P., Kang, H., and Hwangbo, C., "Design of binary masks for extreme ultraviolet lithography with deep ultraviolet inspection by using a simple method," *Journal of the Korean Physical Society* **60**(8), 1305–1309 (2012).